J Nanopart Res (2015) 17:173
DOI 10.1007/s11051-015-2988-3

RESEARCH PAPER

Preparation of carbon-coated $MnFe_2O_4$ nanospheres as high-performance anode materials for lithium-ion batteries

Fei Jiang · Xiumei Du · Saihua Zhao · Jinxin Guo · Bujun Huang · Xiu Huang · Qingmei Su · Jun Zhang · Gaohui Du

Received: 23 January 2015 / Accepted: 1 April 2015 / Published online: 8 April 2015

Abstract Carbon-coated $MnFe_2O_4$ ($MnFe_2O_4$@C) nanospheres were successfully synthesized by a facile two-step method involving the preparation of $MnFe_2O_4$ nanospheres and subsequent pyrolysis treatment. The structure and morphology of the composite were characterized by XRD, SEM, TEM, and HRTEM. The $MnFe_2O_4$ nanospheres with a diameter of 300–400 nm are composed of many nanocrystals (10–15 nm). The surfaces of $MnFe_2O_4$ nanospheres were coated uniformly with thin carbon shells with a thickness of 3–5 nm. The $MnFe_2O_4$@C composites, as anode material for Li-ion battery, showed greatly enhanced electrochemical performance with high lithium storage capacity, satisfactory cyclic durability, and rate capacity compared with the pristine $MnFe_2O_4$. The reversible capacity of the $MnFe_2O_4$@C composites was retained at 646 mAh g^{-1} after 50 cycles at 100 mA g^{-1}. Even when cycled at various rates for 50 cycles, the capacity could recover to 626 mAh g^{-1} at the current of 100 mA g^{-1}. The $MnFe_2O_4$@C nanospheres exhibit excellent electrochemical performance as a potential candidate for anode material in high-energy lithium-ion battery.

Keywords Nanostructures · Composite · Electron microscopy · Anode material

F. Jiang · X. Du · S. Zhao · J. Guo · Q. Su · J. Zhang · G. Du (✉)
Institute of Physical Chemistry, Zhejiang Normal University, Jinhua 321004, China
e-mail: gaohuidu@zjnu.edu.cn

B. Huang · X. Huang
Chuyang Honors College, Zhejiang Normal University, Jinhua 321004, China

Introduction

In recent years, lithium-ion batteries (LIBs) have become the dominant power sources in portable electronic devices and electric vehicles due to their high gravimetric and volumetric capacity, long cycle life, less environmental pollution, etc. (Dunn et al. 2011; Bruce et al. 2008; Xu et al. 2014). Although graphite has served as a reliable anode material for commercial LIBs with high reversibility, its low capacity (372 mAh g^{-1}) can hardly meet the increasing demand for high energy/power density of next-generation LIBs (Zhang et al. 2012a, b). To improve the electrochemical performance of LIBs, considerable efforts have been made recently in finding new electrode materials, which should have higher energy density compared with the existing system (Ji et al. 2011). Transition metal oxides have been widely investigated as anode materials for LIBs because they have higher specific capacity and volumetric energy density than graphite (Zhou et al. 2014; Wang et al. 2011; Zhao et al. 2008; Zhang et al. 2014a, b; Tummala et al. 2012). However, transition metal

oxides suffer from large volume change during lithiation/delithiation process, which leads to poor reversibility and rapid capacity degradation. For example, MnO delivered a capacity of 650 mAh g^{-1} in the first cycle but it decreased quickly to 250 mAh g^{-1} after 20 cycles (Liu et al. 2012); Fe_3O_4 showed a discharge capacity of more than 949 mAh g^{-1} in the first cycle that declined to 200 mAh g^{-1} after 20 cycles (Yoon et al. 2011). To circumvent the poor cycle and high rate problems of transition metal oxides, tremendous efforts have been made to improve their electrochemical performance by optimizing the size of particles, constructing special architectures, coating with electronically conductive layers, or doping metals into compounds (Xu et al. 2014; Zhang et al. 2012a, b; Wang et al. 2011; Issac et al. 2011). Recently, ternary metal oxides have received considerable attention due to their good cyclic stability due to the possible synergistic effect, which enhances the intrinsic properties of each component. For example, $MnCo_2O_4$ quasi-hollow microsphere electrodes exhibited a long cycle life of 610 mAh g^{-1} after 100 cycles (Li et al. 2013). $ZnFe_2O_4$/C electrodes showed a high specific capacity of 840 mAh g^{-1} after 30 cycles (Deng et al. 2011). However, the ternary metal oxides still cannot tolerate high current density. $ZnFe_2O_4$ electrode only maintained a discharge capacity of 86 mAh g^{-1} at high current density of 1600 mA g^{-1} (Xie et al. 2014).

Carbon coating is a simple and effective way to alleviate the above issues (Deng et al. 2011). On one hand, carbon materials are very stable anode materials in LIBs due to their small volume change during Li^+ insertion/extraction. The SEI films on carbon surface are also relatively stable, which further ensure the structural stability upon cycling (Xiao et al. 2013; Hu et al. 2006; Needham et al. 2006; Li et al. 2009). On the other hand, carbon has high conductivity, which greatly enhances the rapid electron transport during the electrochemical Li^+ insertion/extraction reaction (Geng et al. 2014; Zhi et al. 2008). In particular, carbon coatings can serve as perfect barriers to protect the inner active materials and maintain their high capacities (Su et al. 2013; Wang et al. 2010; Lou et al. 2008; Liu et al. 2009; Su et al. 2012).

$MnFe_2O_4$ is an important ternary metal oxide and has been widely investigated in drug delivery (Shah et al. 2013), environmental remediation (Yao et al. 2014), and LIBs (Lin et al. 2013) for its excellent physical and chemical properties. During the past few years, Xiao et al. synthesized $MnFe_2O_4$–graphene nanocomposites by hydrothermal method, which showed an enhanced reversible capacity and an excellent rate capacity (Xiao et al. 2013). Lin et al. successfully synthesized $MnFe_2O_4$ particles with different morphologies including cube, truncated cube, polyhedron, and octahedron (Lin et al. 2013). The polyhedral $MnFe_2O_4$ particles exhibited a large initial discharge capacity of 980 mAh g^{-1} and remained about 428 mAh g^{-1} after 50 cycles, which was large than the other $MnFe_2O_4$ particles. Zhang et al. successfully synthesized mesoporous $MnFe_2O_4$ microspheres which displayed a capacity of 410.3 mAh g^{-1} after 50 cycles at 0.2 C (Zhang et al. 2013a, b). Permien et al. synthesized nanocrystalline $MnFe_2O_4$ by conventional refluxing method and investigated the reaction mechanism of Li^+ insertion into anode materials (Permien et al. 2013). To the best of our knowledge, there are no reports on the studies of carbon-coated $MnFe_2O_4$ ($MnFe_2O_4$@C) composites as anode materials for LIBs. In this paper, we report a facile method for the preparation of $MnFe_2O_4$@C composites, which show good reversible capacity, remarkable rate, and cycling performance for LIBs.

Experimental

Synthesis of $MnFe_2O_4$ nanospheres

All the reagents were of analytical purity and were used without further purification. $MnFe_2O_4$ was prepared by a hydrothermal method. 2.5 mmol manganese acetate tetrahydrate ($Mn(CH_3COO)_2{\cdot}4H_2O$), 5.0 mmol iron chloride hexahydrate ($FeCl_3{\cdot}6H_2O$), 1.0 g polyethylene glycol (PEG), and 3.6 g CH_3-COONa were mixed and dissolved in 40 ml of ethylene glycol (EG) to form a uniform solution. The mixture was transferred into a Teflon-lined autoclave and maintained at 200 °C for 10 h. Finally, the $MnFe_2O_4$ microspheres were obtained after centrifugation and drying at 60 °C overnight.

Synthesis of $MnFe_2O_4$@C composites

The as-prepared $MnFe_2O_4$ nanospheres (0.2 g) were dispersed in 25 mL deionized water by ultrasonication to form a suspension. 0.5 g of glucose was added to the

solution under gentle stirring. The resulting suspension was transferred to a Teflon autoclave (40 mL), which was heated at 200 °C for 12 h. The solid products were separated by centrifugation and dried at 60 °C overnight. The $MnFe_2O_4$@C composites were obtained after calcination at 500 °C in Ar atmosphere for 4 h.

Characterization

X-ray diffraction (XRD) patterns were obtained by a diffractometer (Philips PW3040/60) with Cu Ka radiation ($\lambda = 1.5418$ Å). Raman spectrum was recorded by a Renishaw RM2000 Raman system with He–Ne (632.8 nm) laser excitation. The morphologies of the samples were examined using scanning electron microscopy (SEM, Hitachi S4800), and the microstructures were investigated using high-resolution TEM (HRTEM, JEOL-2100F) performed at an acceleration voltage of 200 kV. The thermogravimetric analysis (TG) measurement of the sample was performed using Netzsch STA 449C thermal analyzer. The carbon percentage in $MnFe_2O_4$@C composites was determined by a Flash EA1112 element analysis analyzer (Thermo Fisher Scientific Inc).

Electrochemical measurement

Electrochemical performances of the as-prepared composites were investigated with two-electrode coin-type cells (CR2025). The working electrodes were prepared by a slurry coating procedure. The slurry consisted of the as-synthesized $MnFe_2O_4$@C composite or pure $MnFe_2O_4$ as active material, acetylene black as conducting additive, and polyvinylidene fluorides (PVDF) as binder with a weight ratio of 75:10:15 in *N*-methyl pyrrolidinone (NMP); the slurry was spread on a nickel foam and dried at 80 °C for 6 h in vacuum. The CR2025-type coin cells were assembled in an argon-filled glove box. The electrolyte solution was 1 M $LiPF_6$ dissolved in a mixture of ethylene carbonate and dimethyl carbonate with a volume ratio of 1:1. The CV experiment was tested on a CHI604D electrochemistry workstation from 0.01 to 3.0 V (vs. Li^+/Li) at a scan rate of 0.1 mV s^{-1}. The galvanostatic charge and discharge measurements were tested at a current density of 100 mA g^{-1}, and the rate performance was conducted at different current densities (100, 200, 500, 1000 mA g^{-1}) with 10 charge–discharge cycles at each step on a battery test system (Neware Co. Ltd., Shenzhen) in the voltage range from 0.005 to 3 V. AC impedance measurements were carried out using a CHI604D electrochemical workstation with a 5 mV sinusoidal voltage in the frequency range from 1 MHz to 0.1 Hz at room temperature. The impedance data were fitted using the ZsimpWin computer program.

Results and discussion

Figure 1 shows the typical XRD patterns of the pristine $MnFe_2O_4$ nanospheres and $MnFe_2O_4$@C composites. All the diffraction peaks in the XRD pattern of pristine $MnFe_2O_4$ can be perfectly indexed to the (220), (311), (400), (422), (333), (440), and (533) planes of face-centered cubic $MnFe_2O_4$ with a lattice constant of $a = 8.511$ Å (JCPDS No. 74-2403). The size of $MnFe_2O_4$ nanoparticles estimated from the Debye–Scherrer formula is about 20 nm. The characteristic peaks of the $MnFe_2O_4$@C composites can also be well indexed as cubic $MnFe_2O_4$. No obvious reflection peaks from other impurities were detected in the as-prepared $MnFe_2O_4$@C composites.

The existence of carbon in the $MnFe_2O_4$@C composites is further confirmed by Raman spectroscopic analysis. As shown in Fig. 2, the two characteristic D and G bands at about 1371 and 1585 cm^{-1} belong to the disordered and graphitic carbon, respectively (Yuan et al. 2011). The peak intensity ratio between D and G (I_D/I_G) can be used to estimate the degree of crystallinity of carbon materials. Here, the

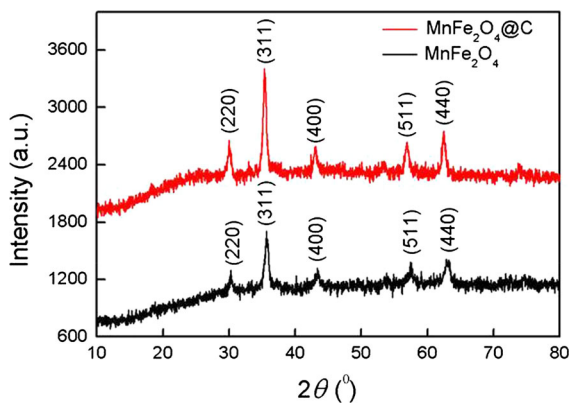

Fig. 1 XRD patterns of the $MnFe_2O_4$ nanospheres and $MnFe_2O_4$@C composites

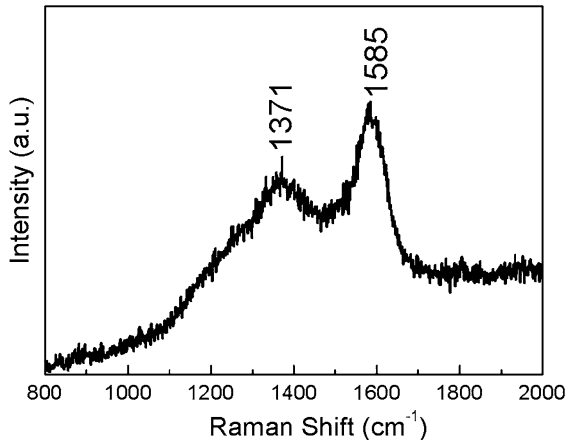

Fig. 2 Raman spectrum of the as-prepared $MnFe_2O_4$@C composites

I_D/I_G value is calculated to be 0.85, indicating that the carbon in these composites is partially graphitized (Zhao et al. 2013).

The carbon content of the as-synthesized $MnFe_2O_4$@C composites was evaluated by thermal gravimetric analysis (TGA) in air (Fig. 3). The TG curves demonstrate that the weight loss of the pristine $MnFe_2O_4$ microspheres is about 3.13 wt% below 100 °C, which is ascribed to the desorption of physically adsorbed H_2O, while the weight loss of 3.27 wt% from 100 to 600 °C is due to the decomposition of organic species (e.g., EG and PEG) adsorbed on the sample surface. The slight weight increase of ~1 wt% from 100 to 250 °C in the TG curve of $MnFe_2O_4$@C sample can be attributed to the

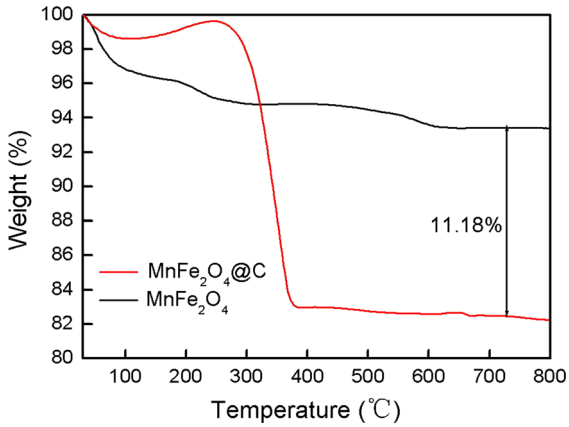

Fig. 3 TG curve of the $MnFe_2O_4$ nanospheres and $MnFe_2O_4$@C composites

rapid formation of C=O functional groups on carbon shells due to the pre-oxidation reaction (Wu et al. 2013), which is similar to the TG result of RGO–$MnFe_2O_4$ nanocomposites (Zhang et al. 2014a, b). The rapid weight loss of $MnFe_2O_4$@C composites appears between 300 and 450 °C, which is attributed to the oxidation of carbon. On the basis of the weight losses, the amount of carbon in the $MnFe_2O_4$@C composites is around 11.18 wt%. To further determine the carbon content of $MnFe_2O_4$@C composites, the elemental analysis experiment was also performed. The carbon content is revealed to be 12.01 wt%, which is well consisted with the TG result.

The morphology and microstructure of the as-prepared products were measured using SEM and TEM. It is very clear that the pristine $MnFe_2O_4$ has a spherical morphology with diameters ranging from 300 to 400 nm (Fig. 4a, b). An HRTEM image (Fig. 4c) of the $MnFe_2O_4$ nanospheres confirms the high crystallinity of $MnFe_2O_4$ nanoparticles. The lattice fringe with a spacing of 0.30 nm is assigned to the (220) plane of cubic $MnFe_2O_4$. As shown in Fig. 4d and e, the spherical morphology is well preserved after pyrolysis treatment for the preparation of $MnFe_2O_4$@C. An HRTEM image of the $MnFe_2O_4$@C nanosphere and its corresponding FFT pattern are shown in Fig. 4f; the lattice fringes of $MnFe_2O_4$ show a spacing of 0.26 nm, which agrees well with the d-spacing of the (311) plane of $MnFe_2O_4$. Also, the carbon layers can be clearly seen in the HRTEM image with a uniform thickness of 3–5 nm, confirming the successful wrapping of thin carbon shells on $MnFe_2O_4$ microspheres.

The formation process and mechanism of $MnFe_2O_4$@C composites is proposed. In the first stage, $MnFe_2O_4$ is nucleated in the presence of Fe^{3+} and Mn^{2+} ions under solvothermal condition via the reaction ($2Fe^{3+} + Mn^{2+} + 4H_2O \rightarrow MnFe_2O_4 + 8H^+$), which leads to the formation of nanosized crystalline $MnFe_2O_4$ (10–15 nm). Then, in the second stage, these nanosized crystallites are self-assembled into large secondary nanospheres, driven by a need to reduce their surface energy. CH_3COONa plays a crucial role as a mineralizer for the formation of $MnFe_2O_4$ nanospheres with a narrow size distribution (Zhang et al. 2012a, b). Ethylene glycol acts as a structure-directing agent to regulate the surface state of the nanosized crystalline particles and influence their nucleation and aggregation process, which are

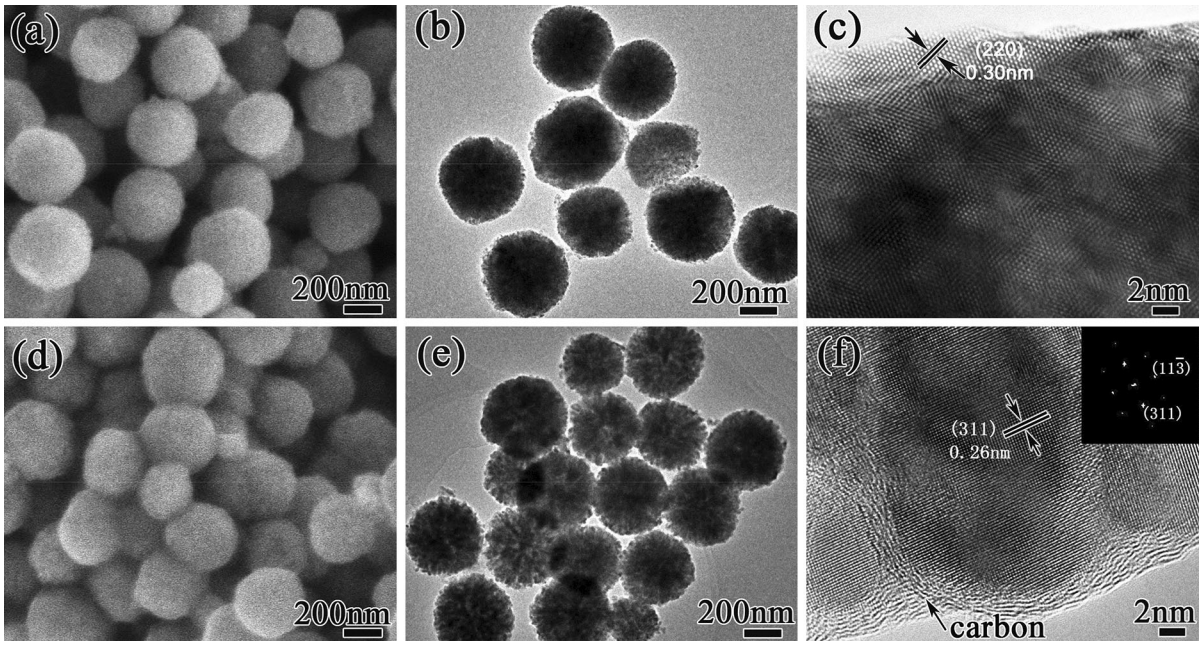

Fig. 4 SEM image (**a**), TEM image (**b**), and HRTEM (**c**) image of $MnFe_2O_4$ nanospheres; SEM image (**d**), TEM (**e**), and HRTEM (**f**), images of $MnFe_2O_4$@C composites and the corresponding FFT pattern (*inset*)

finally assembled into nanospheres (Zhang et al. 2013a, b). Subsequently, carbonaceous materials are produced by hydrothermal carbonization of glucose at low temperature (180–200 °C), which is a well-established method to create hydrophilic carbon materials (Wang et al. 2001). The surfaces of $MnFe_2O_4$ nanosphere with rich hydroxyl groups can induce the in situ precipitation of carbonaceous units to form a uniform carbon shell by carbonization of glucose. In order to improve the stability and electrical conductivity of the carbon shells, they are further graphitized at 500 °C for 4 h in Ar atmosphere. Eventually, the $MnFe_2O_4$@C nanospheres are produced.

The electrochemical reactivity of $MnFe_2O_4$@C composites for lithium storage was evaluated by CV measurement. Figure 5a shows the CV curves of the as-prepared $MnFe_2O_4$@C composite electrode from the first to the fourth cycle between 0.01 and 3.0 V at a scan rate of 0.1 mV s^{-1}. There is a broad peak centered at 0.5 V in the first cathodic process, which is associated with the reduction of Mn^{2+} and Fe^{3+} to Mn^0 and Fe^0, and the formation of SEI film due to the decomposition of the electrolyte (Xiao et al. 2013). Recently, in situ TEM has been used to understand the electrochemical conversion mechanism of $MnFe_2O_4$ in LIBs (Liu et al. 2014). It was found that single-crystalline $MnFe_2O_4$ was converted into polycrystalline Li_2O/Mn/Fe with large volume expansion during the first discharge and subsequently transformed to polycrystalline MnO/Fe_3O_4 with volume shrinkage during charge. Reversible conversion between MnO/Fe_3O_4 and Li_2O/Mn/Fe occurred during the subsequent cycles with small volume changes. The main cathodic peak in Fig. 5a shifts to about 0.8 V from the second cycles, distinguishing the later conversion mechanism from that in the first cycle. During the anodic process, two peaks are present at 1.60 and 1.75 V, which are associated with the oxidation of Mn and Fe to MnO and Fe_3O_4, respectively. Compared with the first discharge process, the peak current and the integrated area of this process decrease, indicating a large capacity loss during the charge process. In the subsequent charging process, two anodic peaks shift to 1.7 and 1.8 V because of the polarization of electrode materials (Tao et al. 2011). The conversion reaction could be described as follows (Liu et al. 2014):

In the first cycle,

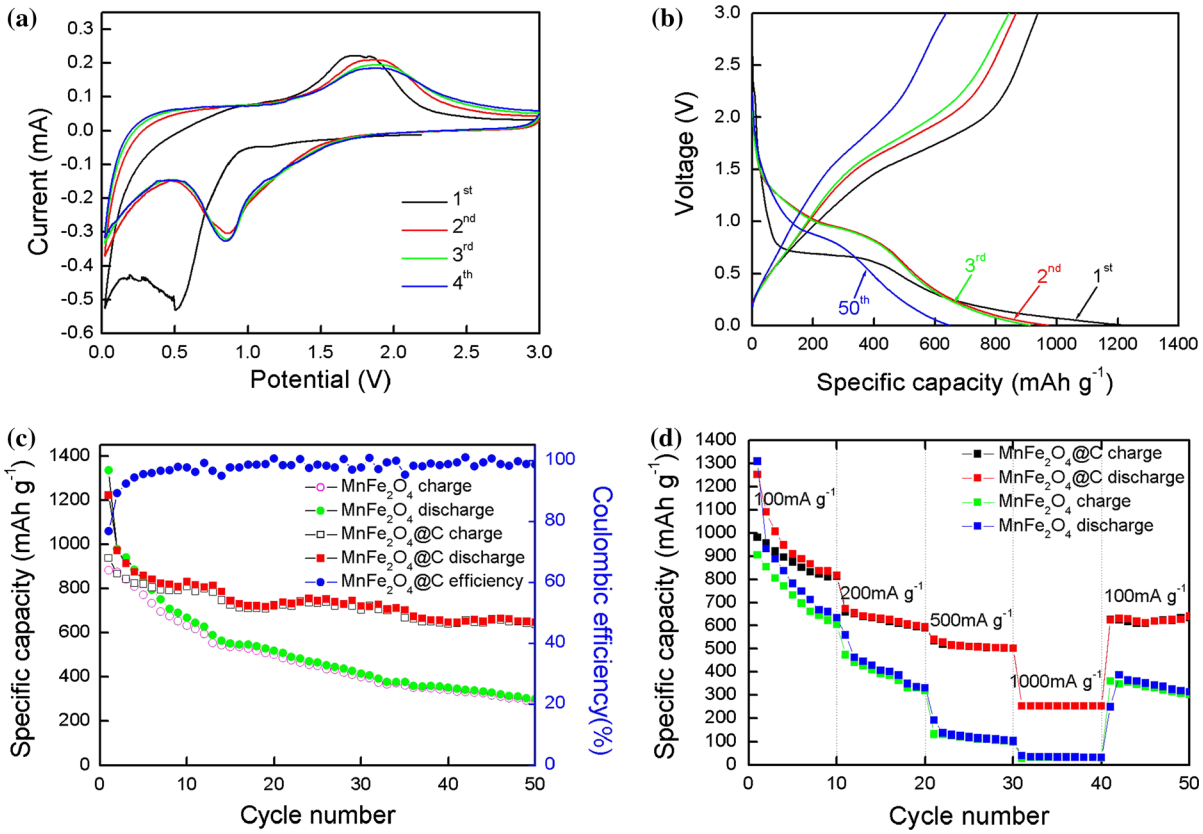

Fig. 5 **a** CV curves of $MnFe_2O_4$@C composites at a scan rate of 0.1 mV s^{-1}. **b** Voltage profiles of $MnFe_2O_4$@C composites for the selected galvanostatic cycles at a current density of 100 mA g^{-1}. **c** Cycling performance of the prepared $MnFe_2O_4$ nanospheres and $MnFe_2O_4$@C composites at a current density of 100 mA g^{-1}. **d** Rate capability of the $MnFe_2O_4$ nanospheres and $MnFe_2O_4$@C composite electrode between 100 and 1000 mA g^{-1}

$$MnFe_2O_4 + 8Li^+ + 8e^- \rightarrow Mn + 2Fe + 4Li_2O \quad (1)$$

$$Mn + Li_2O \rightarrow MnO + 2Li^+ + 2e^- \quad (2)$$

$$3Fe + 4Li_2O \rightarrow Fe_3O_4 + 8Li^+ + 8e^- \quad (3)$$

In the subsequent charge–discharge cycles,

$$Mn + 3Fe + 5Li_2O \leftrightarrow MnO + Fe_3O_4 + 10Li^+ + 10e^- \quad (4)$$

The discharge–charge voltage profiles of the $MnFe_2O_4$@C composites at a current density of 100 mA g^{-1} are shown in Fig. 5b. In the first discharge process, the constant slopes between 0.7 and 0.2 V indicate the conversion reaction from $MnFe_2O_4$ to Mn/Fe and the SEI formation. The discharge plateau shifts to 0.7–1 V from the second cycle, which agrees well with the CV analysis. A plateau at 1.5–2 V during all the charge cycles was recorded. These voltage plateaus were formed due to the reversible oxidation/reduction conversion between Mn/Fe and MnO/Fe_3O_4 during the Li^+ insertion/extraction.

The cycling performance of pristine $MnFe_2O_4$ nanospheres and $MnFe_2O_4$@C composites was measured at a constant current of 100 mA g^{-1} and is shown in Fig. 5c. The $MnFe_2O_4$@C composite electrode delivers a discharge capacity of 1222 mAh g^{-1} and a charge capacity of 938 mAh g^{-1} in the first cycle, which is much larger than the theoretical value of $MnFe_2O_4$ (917 mAh g^{-1}). The initial capacity loss of 23.2 % mainly results from the diverse irreversible process, such as the irreversible phase conversion (Liu et al. 2014), the interfacial lithium storage, and the inevitable formation of SEI layer, which are common for most anode materials (Mai et al. 2011; Xu et al. 2012;

Chen et al. 2012; Tang et al. 2014). However, the Coulombic efficiency reaches 95.5 % after the 5th cycle and remains relatively stable at 98 % in the subsequent cycles. In addition, the $MnFe_2O_4$@C composite retains a capacity of 646 mAh g^{-1} after 50 cycles, which is larger than the capacities of $MnFe_2O_4$ with different morphologies in literature (Lin et al. 2013; Permien et al. 2013). Even though a higher capacity (1335 mAh g^{-1}) can be observed at the first cycle for the pristine $MnFe_2O_4$ microspheres, the capacity decreases quickly to 300 mAh g^{-1} after 50 cycles, showing an obviously poorer performance than $MnFe_2O_4$@C composite.

To investigate the rate capacity of $MnFe_2O_4$@C composites, the electrode was cycled at different current densities. As shown in Fig. 5d, the $MnFe_2O_4$@C composite electrode exhibits a surprising enhancement in rate capacity compared with pristine $MnFe_2O_4$ microspheres. The capacity of $MnFe_2O_4$@C composites is maintained at about 252 mAh g^{-1} at a high current density of 1000 mA g^{-1} after 40 cycles and recovers to 626 mAh g^{-1} when the current density is reduced back to 100 mA g^{-1}. However, the pristine $MnFe_2O_4$ nanospheres deliver only $\sim$40 mAh g^{-1} at the current density of 1000 mA g^{-1}. The poor rate performance is mainly caused by their low electronic conductivity and large volume variations during the charge/discharge process. The carbon shells in $MnFe_2O_4$@C composite can not only enhance the conductivity of the electrode but also serve as protective layers to prevent the inner active materials from pulverizing, and thus maintain their high capacities (Su et al. 2013). The results indicate that the as-prepared $MnFe_2O_4$@C composites could tolerate high current charge–discharge cycling.

To further understand the good rate performance for $MnFe_2O_4$@C composites, electrochemical impedance spectra (EIS) of the pristine $MnFe_2O_4$ nanospheres and $MnFe_2O_4$@C composite electrodes were measured after 50 cycles and are shown in Fig. 6a. The impedance data were fitted using the ZsimpWin computer program. A semicircle followed by a straight line is observed in the EIS spectrum, which is a typical blocking-type behavior of thin-film electrode (Abe et al. 2004). The semicircle at the high-frequency region is assigned to the charge-transfer process of Li^+ ion at the $MnFe_2O_4$/electrolyte interface, while the line in the lower-frequency region is ascribed to the limited diffusion of Li^+ ions into $MnFe_2O_4$. As shown in Fig. 6a, the $MnFe_2O_4$@C electrode exhibits a smaller semicircle compared with the pristine $MnFe_2O_4$, indicating a lower charge-transfer resistance of the $MnFe_2O_4$@C electrode. The equivalent circuit model of the studied system is shown in Fig. 6b to represent the internal resistance of the test battery. The circuit component R_e represents the internal resistance of the test battery, R_{sl} and C_{sl} are designated for the resistance of the migration and capacity of the layer in the high-frequency semicircle, R_{ct} and C_{dl} are associated with the charge-transfer resistance and a double-layer capacitance in the medium-frequency semicircle, Z_W is associated with a Warburg element corresponding to the lithium-ion finite diffusion process (Su et al. 2012; Yang et al. 2010). The fitted impedance parameters are listed in Table 1. It can be seen that R_{sl} of the $MnFe_2O_4$@C electrode is 3.05 Ω, which is significantly lower than that of the pristine $MnFe_2O_4$ (153.5 Ω). This can be attributed to the incorporation of carbon, which has high conductivity, and greatly enhances the electron transport during the electrochemical lithium insertion/extraction reaction. Carbon shell can also prevent the aggregation of $MnFe_2O_4$, resulting in significantly short diffusion path. The charge-transfer

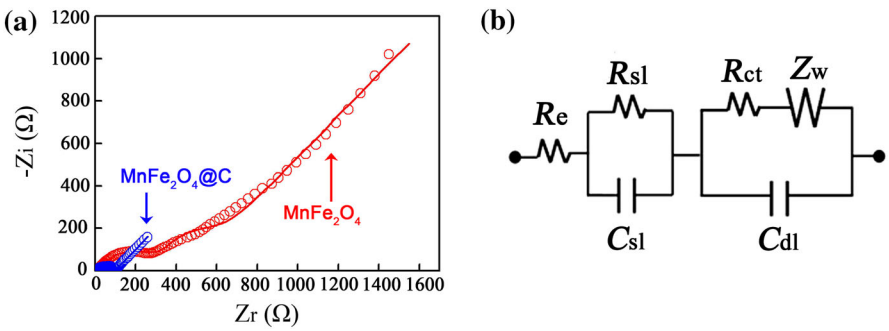

Fig. 6 **a** Electrochemical impedance spectra of the pristine $MnFe_2O_4$ nanospheres and $MnFe_2O_4$@C composite electrodes after the 50th discharge/charge cycle. **b** Equivalent circuit for $MnFe_2O_4$ nanospheres and $MnFe_2O_4$@C composite electrode/electrolyte interface

Table 1 Impedance parameters derived using equivalent circuit model for $MnFe_2O_4$ and $MnFe_2O_4$@C electrodes

Electrode	R_e (Ω)	R_{sl} (Ω)	R_{ct} (Ω)
$MnFe_2O_4$	10.18	153.5	325
$MnFe_2O_4$@C	7.3	3.05	94.2

resistance R_{ct} of the $MnFe_2O_4$@C electrode is 94.2 Ω, while the pristine $MnFe_2O_4$ electrode is 325 Ω. Since the charge-transfer procedure occurs on the contact interface between active material and electrolyte, it is reasonable that $MnFe_2O_4$@C electrode with larger contact interface exhibits smaller R_{ct}. From the above discussion, it is concluded that the total resistance of $MnFe_2O_4$@C electrode is obviously lower than that of the pristine $MnFe_2O_4$ electrode, resulting in the significant improvement in the electrochemical performance.

Conclusion

In summary, we have successfully fabricated the $MnFe_2O_4$@C composites by a scalable solvothermal process with subsequent calcination. The thin carbon shells with a thickness of 3–5 nm are well wrapped on $MnFe_2O_4$ nanospheres. The as-prepared $MnFe_2O_4$@C composites are proved to have a greatly improved electrochemical performance as comparison with the pristine $MnFe_2O_4$, showing excellent cyclic stability and rate performance. This can be attributed to the uniform and continuous carbon layers, which can prevent the aggregation and maintain the integrity of particles, and greatly improve the electronic conductivity of electrodes. Our results reveal a new approach to $MnFe_2O_4$@C composite with great potential as superior anode materials for LIBs.

Acknowledgments This work was supported by the Program for New Century Excellent Talents in University of Ministry of Education of China (NCET-11-1081) and the National Science Foundation of China (No. 21203168).

References

Abe T, Fukuda H, Iriyama Y, Ogumi Z (2004) Solvated Li-ion transfer at interface between graphite and electrolyte. J Electrochem Soc 151:A1120–A1123

Bruce PG, Scrosati B, Tarascon JM (2008) Nanomaterials for rechargeable lithium batteries. Angew Chem Int Ed 47:2930–2946

Chen X, Zhang N, Sun K (2012) Facile ammonia-induced fabrication of nanoporous NiO films with enhanced lithium-storage properties. Electrochem Commun 20:137–140

Deng Y, Zhang Q, Tang S, Zhang L, Deng S, Shi Z, Chen G (2011) One-pot synthesis of $ZnFe_2O_4$/C hollow spheres as superior anode materials for lithium ion batteries. Chem Commun 47:6828–6830

Dunn B, Kamath H, Tarascon JM (2011) Electrical energy storage for the grid: a battery of choices. Science 334:928–935

Geng H, Zhou Q, Zheng J, Gu H (2014) Preparation of porous and hollow Fe_3O_4@C spheres as an efficient anode material for a high-performance Li-ion battery. RSC Adv 4:6430–6434

Hu J, Li H, Huang X, Chen L (2006) Improve the electrochemical performances of Cr_2O_3 anode for lithium ion batteries. Solid State Ion 177:2791–2799

Issac I, Scheuermann M, Becker SM, Bardají EG, Adelhelm C, Wang D, Kübel C, Indris S (2011) Nanocrystalline $Ti_{2/3}Sn_{1/3}O_2$ as anode material for Li-ion batteries. J Power Sources 196:9689–9695

Ji L, Lin Z, Alcoutlabi M, Zhang X (2011) Recent developments in nanostructured anode materials for rechargeable lithium-ion batteries. Energy Environ Sci 4:2682–2699

Li H, Wang Z, Chen L, Huang X (2009) Research on advanced materials for li-ion batteries. Adv Mater 21:4593–4607

Li J, Xiong S, Li X, Qian Y (2013) A facile route to synthesize multiporous $MnCo_2O_4$ and $CoMn_2O_4$ spinel quasi-hollow spheres with improved lithium storage properties. Nanoscale 5:2045–2054

Lin X, Lv X, Wang L, Zhang F, Duan L (2013) Preparation and characterization of $MnFe_2O_4$ in the solvothermal process: their magnetism and electrochemical properties. Mater Res Bull 48:2511–2516

Liu J, Li Y, Ding R, Jiang J, Hu Y, Ji X, Chi Q, Zhu Z, Huang X (2009) Carbon/ZnO nanorod array electrode with significantly improved lithium storage capability. J Phys Chem C 113:5336–5339

Liu SY, Xie J, Zheng YX, Cao GS, Zhu TJ, Zhao XB (2012) Nanocrystal manganese oxide (Mn_3O_4, MnO) anchored on graphite nanosheet with improved electrochemical Li-storage properties. Electrochim Acta 66:271–278

Liu SY, Xie J, Su QM, Du GH, Zhang SC, Cao GS, Zhu TJ, Zhao XB (2014) Understanding Li-storage mechanism and performance of $MnFe_2O_4$ by in situ TEM observation on its electrochemical process in nano lithium battery. Nano Energy 8:84–94

Lou XW, Deng D, Lee JY, Archer LA (2008) Preparation of SnO_2/carbon composite hollow spheres and their lithium storage properties. Chem Mater 20:6562–6566

Mai YJ, Wang XL, Xiang JY, Qiao YQ, Zhang D, Gu CD, Tu JP (2011) CuO/graphene composite as anode materials for lithium-ion batteries. Electrochim Acta 56:2306–2311

Needham SA, Wang GX, Konstantinov K, Tournayre Y, Lao Z, Liu HK (2006) Electrochemical performance of Co_3O_4–C composite anode materials. Electrochem Solid State Lett 9:A315–A319

Permien S, Hain H, Scheuermann M, Mangold S, Mereacre V, Powell KA, Indris S, Schürmann U, Kienle L, Duppel V,

Harm S, Bensch W (2013) Electrochemical insertion of Li into nanocrystalline MnFe2O4: a study of the reaction mechanism. RSC Adv 3:23001–23014

Shah SA, Majeed A, Rashid K, Awan SU (2013) PEG-coated folic acid-modified superparamagnetic $MnFe_2O_4$ nanoparticles for hyperthermia therapy and drug delivery. Mater Chem Phys 138:703–708

Su Y, Li S, Wu D, Zhang F, Liang H, Gao P, Cheng C, Feng X (2012) Two-dimensional carbon-coated graphene/metal oxide hybrids for enhanced lithium storage. ACS Nano 6:8349–8356

Su QM, Du GH, Zhang J, Zhong YJ, Xu BS, Yang YH, Neupane S, Kadel K, Li WZ (2013) In situ transmission electron microscopy investigation of the electrochemical lithiation-delithiation of individual Co_9S_8/Co-filled carbon nanotubes. ACS Nano 7:11379–11387

Tang H, Gao PB, Xing A, Tian S, Bao ZH (2014) One-pot low-temperature synthesis of a $MnFe_2O_4$–graphene composite for lithium ion battery applications. RSC Adv 4:28421–28425

Tao HC, Fan LZ, Mei Y, Qu X (2011) Self-supporting Si/reduced graphene oxide nanocomposite films as anode for lithium ion batteries. Electrochem Commun 13:1332–1335

Tummala R, Guduru RK, Mohanty PS (2012) Binder free, porous and nanostructured Co_3O_4 anode for Li-ion batteries from solution precursor plasma deposition. J Power Sources 199:270–277

Wang Q, Li H, Chen LQ, Huang XJ (2001) Monodispersed hard carbon spherules with uniform nanopores. Carbon 39:2211–2214

Wang Y, Zhang HJ, Lu L, Stubbs LP, Wong CC, Lin J (2010) Designed functional systems from peapod-like Co@Carbon to Co_3O_4@Carbon nanocomposites. ACS Nano 4:4753–4761

Wang B, Chen JS, Wu HB, Wang Z, Lou XW (2011) Quasiemulsion-templated formation of α-Fe_2O_3 hollow spheres with enhanced lithium storage properties. J Am Chem Soc 133:17146–17148

Wu H, Fan SW, Yuan XW, Chen LF, Deng JL (2013) Fabration of carbon fibers from jute fibers by peroxidation and carbonization. New Carbon Mater 28:448–453

Xiao Y, Zai J, Tao L, Li B, Han Q, Yu C, Qian X (2013) $MnFe_2O_4$–graphene nanocomposites with enhanced performances as anode materials for Li-ion batteries. Phys Chem Chem Phys 15:3939–3945

Xie J, Song W, Cao G, Zhu T, Zhao X, Zhang S (2014) One-pot synthesis of ultrafine $ZnFe_2O_4$ nanocrystals anchored on graphene for high-performance Li and Li-ion batteries. RSC Adv 4:7703–7709

Xu X, Cao R, Jeong S, Cho J (2012) Spindle-like mesoporous α-Fe_2O_3 anode material prepared from MOF template for high-rate lithium batteries. Nano Lett 12:4988–4991

Xu LL, Bian SW, Song KL (2014) Graphene sheets decorated with ZnO nanoparticles as anode materials for lithium ion batteries. J Mater Sci 49:6217–6224

Yang S, Feng X, Ivanovici S, Mullen K (2010) Fabrication of graphene-encapsulated oxide nanoparticles: towards high-performance anode materials for lithium storage. Angew Chem Int Ed 49:8408–8411

Yao Y, Cai Y, Lu F, Wei F, Wang X, Wang S (2014) Magnetic recoverable $MnFe_2O_4$ and $MnFe_2O_4$–graphene hybrid as heterogeneous catalysts of peroxymonosulfate activation for efficient degradation of aqueous organic pollutants. J Hazard Mater 270:61–70

Yoon T, Chae C, Sun YK, Zhao X, Kung HH, Lee JK (2011) Bottom-up in situ formation of Fe_3O_4 nanocrystals in a porous carbon foam for lithium-ion battery anodes. J Mater Chem 21:17325–17330

Yuan SM, Li JX, Yang LT, Su LW, Liu L, Zhou Z (2011) Preparation and lithium storage performance of mesoporous Fe_3O_4@C microcapsules. ACS Appl Mater Inter 3:705–709

Zhang C, Wang Z, Guo Z, Lou XW (2012a) Synthesis of MoS_2-C one-dimensional nanostructures with improved lithium storage properties. ACS Appl Mater Inter 4:3765–3768

Zhang ZL, Che HW, Wang YL, Gao JJ, She XL, Sun J, Zhong ZY, Su FB (2012b) Flower-like CuO microspheres with enhanced catalytic performance for dimethyldichlorosilane synthesis. RSC Adv 2:2254–2256

Zhang Z, Wang Y, Tan Q, Zhong Z, Su F (2013a) Facile solvothermal synthesis of mesoporous manganese ferrite ($MnFe_2O_4$) microspheres as anode materials for lithium-ion batteries. J Colloid Interface Sci 398:185–192

Zhang ZL, Wang YH, Zhang MJ, Tan QQ, Lv X, Zhang ZY, Su FB (2013b) Mesoporous $CoFe_2O_4$ nanospheres cross-linked by carbon nanotubes as high-performance anodes for lithium-ion batteries. J Mater Chem A 1:7444–7464

Zhang L, Wu HB, Lou XW (2014a) Iron-oxide- based advanced anode materials for lithium ion batteries. Adv Energy Mater 4:1300958

Zhang XJ, Wang GS, Cao WQ, Wei YZ, Liang JF, Guo L, Cao MS (2014b) Enhanced microwave absorption property of reduced graphene oxide (RGO)-$MnFe_2O_4$ nanocomposites and polyvinylidene fluoride. ACS Appl Mater Interface 6:7471–7478

Zhao N, Wang G, Huang Y, Wang B, Yao B, Wu Y (2008) Preparation of nanowire arrays of amorphous carbon nanotube-coated single crystal SnO_2. Chem Mater 20:2612–2614

Zhao NQ, Wu S, He CN, Wang ZY, Shi CS, Liu EZ, Li JJ (2013) One-pot synthesis of uniform Fe_3O_4 nanocrystals encapsulated in interconnected carbon nanospheres for superior lithium storage capability. Carbon 57:130–138

Zhi L, Hu YS, Hamaoui BE, Wang X, Lieberwirth I, Kolb U, Maier J, Müllen K (2008) Precursor-controlled formation of novel carbon/metal and carbon/metal oxide nanocomposites. Adv Mater 20:1727–1731

Zhou XY, Shi JJ, Liu Y, Su QM, Zhang J, Du GH (2014) Microwave irradiation synthesis of Co_3O_4 quantum dots/-graphene composite as anode materials for Li-ion battery. Electrochim Acta 143:175–179